Brain Pathology ISSN 1015-6305

RESEARCH ARTICLE

Distribution of tau hyperphosphorylation in canine dementia resembles early Alzheimer's disease and other tauopathies

Ajantha Abey[1,2]; Danielle Davies[2,3]; Claire Goldsbury[2,3]; Michael Buckland[4,5]; Michael Valenzuela[1,2,6]; Thomas Duncan[1,2,7,*]

[1] Regenerative Neuroscience Group, The Brain and Mind Centre, Faculty of Medicine and Health, University of Sydney, Camperdown, NSW Australia.
[2] Discipline of Anatomy and Histology, School of Medical Sciences, Faculty of Medicine and Health, University of Sydney, Sydney, NSW Australia.
[3] Alzheimer's Disease Cell Biology Research Lab, The Brain and Mind Centre, Faculty of Medicine and Health, University of Sydney, Sydney, NSW Australia.
[4] Department of Neuropathology, Royal Prince Alfred Hospital, Camperdown, NSW Australia.
[5] Sydney Medical School, Brain and Mind Centre, University of Sydney, Sydney, NSW Australia.
[6] School of Psychiatry, Medicine, University of New South Wales, Sydney, NSW Australia.
[7] Department of Anatomy, School of Medical Sciences, University of New South Wales, Sydney, NSW Australia.

Keywords
canine cognitive dysfunction, tau, tauopathy, Alzheimer's disease, Papez circuit, Braak staging, thalamus, serine 396, dementia, Hippocampus.

Abbreviations
Aβ, amyloid-β; AD, Alzheimer's disease; B3T, β-3-tubulin; CCD, canine cognitive dysfunction; CCDR, canine cognitive dysfunction rating; FDR, false discovery rate; GFAP, glial fibrillary acidic protein; MBP, myelin basic protein; NFT, neurofibrillary tangle; PHF, paired helical filament; p-tau, phosphorylated tau; S396, serine residue 396.

Corresponding author:
Thomas Duncan, Department of Anatomy, School of Medical Sciences, University of New South Wales, NSW, Australia (E-mail: *t.duncan@unsw.edu.au*)

Received 7 April 2020
Accepted 12 August 2020
Published Online Article
Accepted 18 August 2020

doi:10.1111/bpa.12893

Abstract

Some aged community dogs acquire a degenerative syndrome termed Canine Cognitive Dysfunction (CCD) that resembles human dementia because of Alzheimer's Disease (AD), with comparable cognitive and behavioral deficits. Dogs also have similar neuroanatomy, share our domestic environment and develop amyloid-β plaques, making them likely a valuable ecological model of AD. However, prior investigations have demonstrated a lack of neurofibrillary tau pathology in aged dogs, an important hallmark of AD, though elevated phosphorylated tau (p-tau) at the Serine 396 (S396) epitope has been reported in CCD. Here using enhanced immunohistochemical methods, we investigated p-tau in six CCD brains and six controls using the AT8 antibody (later stage neurofibrillary pathology), and an antibody against S396 p-tau (earlier stage tau dysfunction). For the first time, we systematically assessed the Papez circuit and regions associated with Braak staging and found that all CCD dogs displayed elevated S396 p-tau labeling throughout the circuit. The limbic thalamus was particularly implicated, with a similar labeling pattern to that reported for AD neurofibrillary pathology, especially the anterior nuclei, while the hippocampus exhibited dysfunction confined to synaptic layers and efferent pathways. The cingulate and temporal lobes displayed significantly greater tauopathy than the frontal and occipital cortices, also reflective of early Braak staging patterns in AD. Immunofluorescence confirmed that S396 was accumulating within neuronal axons, somata and oligodendrocytes. We also observed AT8 labeling in one CCD brain, near the transentorhinal cortex in layer II neurons, one of the first regions to be affected in AD. Together, these data demonstrate a concordance in regional distribution of tauopathy between CCD and AD, most evident in the limbic thalamus, an important step in further validating CCD as a translational model for human AD and understanding early AD pathogenic mechanisms.

INTRODUCTION

Approximately 14% of pet dogs over the age of eight will naturally develop a neurobehavioral syndrome akin to dementia, termed canine cognitive dysfunction (CCD). Characterized by deficits in cognitive function, especially amnesia and spatial orientation, as well as agitation, sleep–wake cycle disruption and dysnosmia, CCD is clinically reminiscent of dementia of Alzheimer's disease (AD) etiology (36,37). Apart from syndromal similarity, community dogs share the human domestic environment and have comparable neuroanatomy to humans, especially with respect to organization of the hippocampus (19,29,36). Thus, CCD may represent a promising naturalistic translational model of AD dementia (32,56).

Hallmarks of human AD include aggregation and deposition of amyloid-β (Aβ) as extracellular plaques and hyperphosphorylation of the microtubule-associated tau protein which aggregates as intracellular neurofibrillary tangles

(NFTs). CCD post-mortem studies have found high levels of Aβ plaques, with a spatial distribution akin to that seen in early stage AD (12,15,20,56). By contrast, prior work suggests a more significant difference between that CCD and AD in terms of tauopathy.

Physiological tau is mostly confined to neuronal axons where it binds and stabilizes microtubules. Microtubule binding and other tau functions are regulated by serine, threonine and tyrosine phosphorylation at different domains within the protein sequence (22,44). In AD, tau is hyperphosphorylated and mislocalized to the somatodendritic compartment, where it aggregates into NFTs (49). Mechanistically, tau dysfunction may include destabilization of microtubules and cytoskeletal breakdown as phosphorylated tau (p-tau) has lower microtubule binding affinity; mis-localization of tau would also reduce its availability for functions in the axon (49,54). Hyperphosphorylation of tau also promotes oligomerization, and these oligomeric species are thought to lead to mitochondrial damage and neurodegeneration *per se* (23,42). Alternatively, *de novo* tau synthesis induced by Aβ oligomers may be implicated (4,27). Importantly, hyperphosphorylation and NFT develops in a highly stereotyped spatiotemporal pattern throughout the brain as described by Braak staging, in a manner closely related to the emergence of clinical symptoms (8,10).

Previous CCD studies have assessed tauopathy by routine immunohistochemical staining. The most commonly employed antibody is the AT8 clone, a standard marker in human pathology studies, as it targets the S202 and T205 phospho-epitopes that are hyperphosphorylated on tau in NFTs. Using this, studies have reported AD-related tauopathy is absent in aged colony dogs (13,16) and is present in <10% of CCD dogs (40,43). However, a small number of studies have also examined a variety of tau phospho-epitopes that may mark earlier stages of tau pathology.

In humans, hyperphosphorylation of tau at the S396 residue occurs earlier than at the AT8 epitope (5,18,30), and has been associated with tau oligomerization in human cells (47). Accordingly, S396 may identify earlier stages of tau dysfunction in neuronal cell bodies and processes prior to PHF or NFT formation. In CCD, elevated levels of S396 p-tau have been found in hippocampal and frontal cortex synaptosomes (43), and intraneuronal accumulations in the parietal cortex and dorsal hippocampus have also been observed (57). Pugliese, Mascort, Mahy and Ferrer (33) also found significantly higher $S396^{+}$ p-tau immunoreactivity in the prefrontal cortex of CCD dogs compared to healthy controls, and changes in the subcellular localization of tau with age. These studies thus indicate that early stage tauopathy is present in CCD.

Prior work has focused on brain regions associated with Braak staging, especially the hippocampus. While this is classically considered the centre of AD-related pathology, Braak and Braak's seminal paper also highlights the thalamus as one of the earliest regions to become affected by tauopathy (10). Recent studies further highlight the Papez circuit, which links the hippocampus, thalamus and cingulate cortex, as critical for episodic memory function and critical to cognitive dysfunction in AD dementia (3). In this study, we therefore, for the first time, systematically assess the Papez circuit for tauopathy in addition to neocortical regions typically associated with later stage disease. Combining both early and late stage tau pathology markers will allow a more complete understanding of the relevance of CCD to human AD modeling.

MATERIALS AND METHODS

Dogs

This study was performed on the brains of six CCD dogs and six healthy controls (Table 1). All procedures were performed in accordance with New South Wales and Australian law. The brains were acquired through donation with owner's consent for research use at the time of elective euthanasia. Dogs were of various breeds but of similar size and age as it has been shown that these, not breed, are the important factors in CCD prevalence (36). Full medical history of the six CCD dogs revealed no neurological comorbidities and included assessment of the dog's cognitive status and

Table 1. CCD dog subjects and dementia behaviors.

Canine #	1	2	3	4	5	6
Sex	Female	Male	Female	Female	Male	Female
Breed	Toy Fox Terrier	Whippet	Terrier Cross	Jack Russel Terrier	Silkie Terrier	Kelpie Cross
Post-mortem Delay (Hours)	1.5	2	<4	<4	3	<4
Age	16	14	17	16	15	16
CCDR	65	72	62	69	60	58
Pacing	4	5	5	5	5	5
Wall Staring	4	5	5	5	5	5
Getting Stuck Behind Objects	4	5	5	5	5	3
Failure to Recognize People/Animals	3	5	1	3	4	4
Walking into Objects	1	5	5	5	5	2
Touch Avoidance	5	5	5	4	5	4
Difficulty Finding Food	3	2	5	5	5	2

All CCD dogs examined in the study are listed below, including their age and canine cognitive dysfunction rating (CCDR), as per Salvin, McGreevy, Sachdev and Valenzuela (37). Canines diagnosed with CCD were assessed using the CCDR on a number of different dementia-related behaviors. These are presented below for the six CCD dogs examined in this study, scored on a scale of 1–5, as per Salvin, McGreevy, Sachdev and Valenzuela (37).

CCD behavioral severity using the Canine Cognitive Dysfunction Rating (CCDR) scale (37) (Table 1). The CCDR scale assessess the core clinical features of CCD, including frequency, severity and rate of changes of abnormal behaviors including pacing and locomotion, owner recognition and interaction, wall staring and olfaction. These are summed to produce a global clinical score that ranges from 0 to 39 (normal), 40 to 49 (at risk) and 50 to 80 (CCD). The CCDR has been validated against clinical veterinary diagnosis in a large study (N ~ 1000) and externally recommended for clinical use (37). Cadavers of control dogs, grayhounds approximately 10 years of age who had undergone elective euthanasia, were obtained from donation through the University of Sydney, Faculty of Veterinary Science.

Tissue processing

All CCD dogs underwent brain extraction within 4 h postmortem. Brains were bisected into hemispheres. One was cut into 4-mm thick sections, snap frozen in isopentane at −80 °C then stored at −80°C. The remaining hemisphere was immersion fixed in 4% paraformaldehyde for 7 days before being cut coronally into 4-mm thick sections. Regions of interest were then dissected out, embedded into paraffin blocks and sectioned at 10 μm thickness for EnVision™ immunohistochemistry, and at 20 μm thickness for fluorescence immunohistochemistry.

EnVision™ Immunohistochemistry

EnVision™ immunohistochemistry was used to visualize both p-tau S396 and AT8 labeled sections (35,48). Sections were dewaxed in xylene and rehydrated through graded ethanols, before undergoing antigen retrieval in 0.01 M citric acid (Sigma-Aldrich, Castle Hill, NSW, Australia) for 10 mins at 95ºC with 0.05% Tween (Sigma). Blocking of non-specific labeling was performed with 10% donkey serum in Tris buffered saline with 0.05% Tween (TBST) (Sigma). Alternating adjacent sections were incubated for 1 h at room temperature in primary antibodies against either p-tau S396 (Ab109390; Abcam) (three sections) or PHF Tau (MN1020; Invitrogren) (three sections), both diluted 1:500 in TBST with 1% donkey serum (Table 2), or TBST with 1% donkey serum only as a no-primary antibody control (one section). Sections were then washed in TBST and stained according to manufacturer instructions (EnVision™ G2 System/AP, Rabbit/Mouse (Permanent Red) Kit, Dako). Sections were then lightly counterstained with hematoxylin, dehydrated through graded ethanol followed by xylene, and mounted with DPX. For more detailed experimental procedures see Supporting Methods.

Fluorescence immunohistochemistry

Sections underwent dewaxing, rehydration and antigen retrieval as above, followed by permeabilization in 0.1% Triton (Sigma) in phosphate buffered saline (PBS) (Sigma) for 10 mins and blocking in 10% donkey serum in TBST for one hour. Sections were then incubated overnight at 4°C with S396 p-tau primary antibody along with a primary antibody against either glial fibrillary acidic protein (GFAP; astrocyte marker), Iba-1 (microglial marker), β-3 tubulin (B3T; neuronal marker), myelin basic protein (MBP) or O4 (oligodendrocyte markers). See Table 2 for more details. Sections were then washed in TBST and incubated for 75 minutes with Alexa fluorophore conjugated secondary antibodies (1:400). Finally, slides were counterstained with NucBlue LiveCell probe (Thermo Fisher Scientific) and mounted with Faramount aqueous mounting medium (Dako).

Imaging and analysis

EnVision™ immunohistochemistry was imaged using an Olympus VS-120 Slide Scanner (Olympus-life science, Shinjuku, Tokyo, Japan) under 40x objective magnification. Regions of interest were defined at acquisition using the freehand drawing tool. These were: (i) the hippocampal formation including entorhinal cortex, (ii) the thalamus at the level of the anterior nucleus, (iii) internal capsule at the level of the anterior thalamic nucleus, (iv) the mamillary body, (v) the anterior cingulate cortex and cingulum bundle, (vi) the prefrontal lobe, (vii), temporal lobe (at the level of the mid thalamus) (viii) occipital lobe (approximately 6 mm from the occipital pole) and (ix) cerebellum. Only S396 p-tau labeling was performed in the mammillary bodies, cingulate lobe and cerebellum. All cortical regions also contained adjacent subcortical white matter, and cortical gray and white matter were analyzed together. Double immunofluorescence was imaged using a Nikon C2 confocal microscope.

Automated area quantification was performed for EnVision™ immunolabeled sections using a custom macro in Fiji software (National Institute of Health) (39) in a manner adapted from Sankaranarayanan (38) and Dai (14). Briefly, custom color deconvolution was performed to separate permanent red tau labeling and hematoxylin staining. Threshold analysis was performed to assess immunolabeling at low, intermediate and high intensity thresholds for S396, with high intensity corresponding to densely accumulated S396 deposits (Figure S1, Supporting File 1). Total stained pixels for each threshold were counted to obtain a percentage area of tissue immunolabeled, as a measure of pathological severity. Images were tiled to apply this analysis across the whole tissue region. Detailed analysis methods are available in Supporting Methods. Pathological severity in more specific structures was also semi-quantitatively assessed by inspection on a five-point scale, blind to clinical status (Figure S2, Supporting File 1).

Statistical analysis

Statistical analysis was performed in GraphPad Prism (GraphPad Software Inc., San Diego, CA, USA). Area immunolabeled for each tissue section in each dog was normalized to a no-primary antibody control for that dog's brain region, and the signal from each region of interest was normalized to signal from the cerebellum of the same dog. Global difference in p-tau between CCD and non-CCD groups based on EnVision™ immunohistochemistry was calculated by comparing the mean labeling across regions for all dogs using

Table 2. Antibodies used for envision™ immunohistochemistry and immunofluorescence

Experiment	Target (clone)	Clonality	Host	Dilution	Source	Cat. Number
EnVision™ IHC	PHF Tau (AT8)	Monoclonal	Mouse	1:500	Invitrogen*	MN1020
EnVision™ IHC and Fluorescence	p-tau S396	Monoclonal	Rabbit	1:500	Abcam†	Ab109390
Western Blotting	p-tau S396	Monoclonal	Rabbit	1:10,000	Abcam†	Ab109390
Fluorescence	GFAP (SMI-22)	Monoclonal	Mouse	1:500	BioLegend‡	835301
Fluorescence	Iba-1	Polyclonal	Goat	1:200	Abcam†	Ab5076
Fluorescence	B3T (TUJ1)	Monoclonal	Mouse	1:500	BioLegend‡	801201
Fluorescence	MBP	Monoclonal	Mouse	1:500	Abcam†	Ab24567
Fluorescence	O4	Monoclonal	Mouse	1:100	Merck§	MAB345A4
Western Blotting	B-actin	Monoclonal	Mouse	1:3000	Sigma¶	A1978

*Rockford, Illinois, USA.
†Location Unavailable.
‡San Diego, California, USA.
§Temecula, California, USA.
¶Castle Hill, NSW, Australia.

the two-tailed Wilcoxon signed rank test. Comparisons in area labeled within and between groups for all regions were performed using two-way ANOVAs with the false discovery rate (FDR) (Benjamini–Hochberg–Yekutieli procedure, Q = 0.05) correction method for multiple comparisons.

Western blotting

From the snap frozen brain sections, tissue biopsies were extracted from nine different regions of interest (ventral hippocampus, anterior thalamic nucleus, gray and subcortical white matter of the temporal, frontal, occipital and cingulate cortices, fornix, internal capsule and cerebellum), matched to immunolabeled areas in the opposite hemisphere. This tissue was then resuspended in RIPA buffer (10 ul/mg) containing 150 nM NaCl, 1% Triton X-100, 0.5% sodium deoxycholate, 5mM EDTA, 0.1% SDS and 50 mM Tris, with Complete Protease Inhibitor and PhosStop inhibitors (50uL/mL). Tissue was then dissociated by trituration and left on ice for 30 mins before being spun at 16,000 *g* at 4°C for 20 mins. Protein extracted in the supernatant plus Novex Sharp LC5800 standard was loaded in a 10 % SDS-polyacrylamide gel for electrophoresis. Proteins were then transferred to a nitrocellulose membrane using a BioRad semi-dry transfer system. The membrane was blocked in 5 % milk powder before incubation with anti-p-tau S396 primary antibody (ab109390, Abcam) overnight, followed by washing and incubation with anti-mouse or anti-rabbit HRP (1:5000). (We did not observe $AT8^+$ p-tau by western blotting (data not shown), consistent with the sparse labeling shown in the immunohistochemistry data). One gel was performed for each dog, including all nine brain regions and a positive chick brain control. Antibody labeling was visualized with ImmunoHRP detection kit and developed using a Bio-rad Chemidoc XRS system with an exposure of 100 s. Membranes were reprobed following this for β-actin as a loading control (Table 2), with a 1-h primary antibody incubation time. Western blotting was performed for all six CCD dogs, and non-CCD Canine 7. Blotting was not performed on Canine 6 internal capsule or cingulate lobe or other non-CCD dogs as fresh frozen tissue was unavailable.

Western blotting analysis

Images were processed with the Gel Analyzer Plugin in Fiji. Lanes were selected and total intensity for S396 p-tau peaks were measured. Background was also measured and subtracted from measured values which were also normalized to the β-actin loading control. S396 p-tau labeling was further baselined to cerebellum. Data analysis was also performed in GraphPad Prism, and comparison in intensity between analyzed regions and the cerebellum was performed by one-way ANOVA using the FDR (Benjamini–Hochberg–Yekutieli procedure, Q = 0.05) correction method for multiple comparisons.

RESULTS

AT8 immunolabeling is sparse and restricted to superficial layers of the inferior temporal lobe in CCD

$AT8^+$ neurons were sparsely observed using EnVision™ labeling in one CCD dog (Canine 3 – Figure 1). This labeling was limited to neuronal somata, consistent with an abnormal distribution of p-tau. The immunoreactive neurons were found in superficial Layer II of the composite gyrus, a region of the canine cortex in the inferior temporal lobe located immediately lateral to the transentorhinal cortex (52). Other CCD and non-CCD dogs were $AT8^-$ in this and all other regions evaluated (Figure S3, Supporting File 1).

CCD dogs show elevated levels of S396 p-tau Immunoreactivity across diverse brain regions

In contrast to AT8 labeling, which is considered a relatively late stage marker of tau-related changes in AD, other p-tau epitopes may reflect earlier stage abnormalities in tau phosphorylation and distribution. We therefore evaluated $S396^+$ p-tau immunoreactivity in CCD and control dogs using EnVision™ immunohistochemistry and western blotting across all nine brain regions. Labeling in each region is summarized

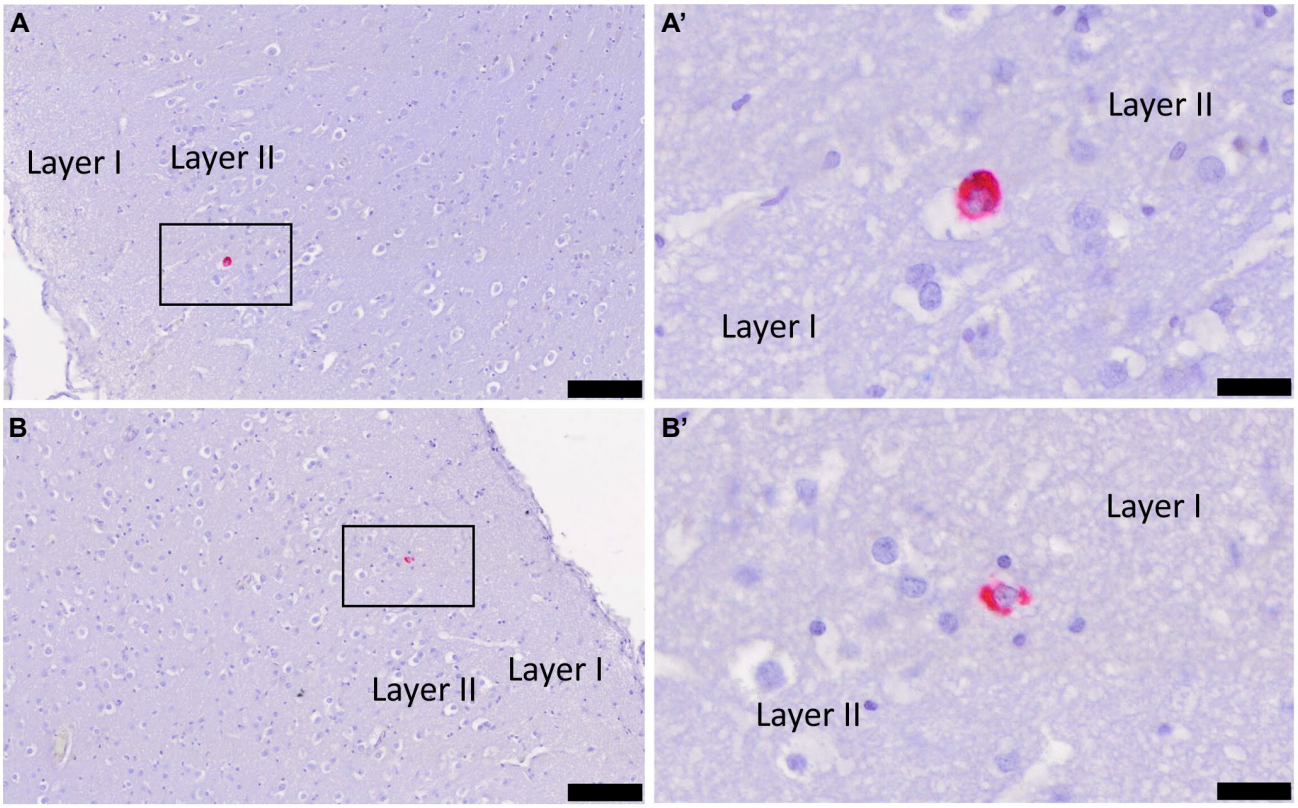

Figure 1. AT8$^+$ labeling in the inferior temporal cortex of canine 3. AT8 labeling was observed through EnVision™ Immunoreactivity in select neurons of Layer II in the composite gyrus in the inferior temporal cortex of Canine 3, just lateral to the transentorhinal cortex. A′ and B′ represent the boxed areas in a and b. Scale bar represents 100 μm (Boxed Areas: 20 μm). Negative control images are available in Figure S3. [Colour figure can be viewed at wileyonlinelibrary.com]

in Table 3. (An extended table is available in Supporting File 1).

Western blotting of CCD brains indicated significantly elevated S396 p-tau in all assessed regions except the hippocampi of CCD dogs, using the cerebellum as internal control (Frontal Lobe: $P = 0.0012$; Internal Capsule: $P = 0.0012$; Thalamus: $P = 0.0023$; Cingulate Lobe: $P = 0.0062$, Occipital Lobe: $P = 0.0086$; Fornix: $P = 0.009$; Temporal Lobe: $P = 0.0132$; Hippocampus: $P = 0.1041$) (Figure 2A,B). At the group level, western blot measure of S396 p-tau was substantially higher across all brain regions in CCD dogs compared to the healthy aged control, and this was corroborated by finding significantly greater histological mean immunolabeling intensity across all regions in the CCD dogs compared to healthy controls (Figure 2D). Full statistical results are available in Supporting File 2.

Hippocampal p-tau immunolabeling predominates in white matter and synaptic layers

In all CCD dogs, S396$^+$ labeling was observed in the ventral hippocampal formation (Figure 2). Some intraneuronal S396$^+$ labeling in the CA1-CA3 and subicular regions of the stratum pyramidale was evident in Canine 5 (Figure 3B,C), though the other five CCD brains displayed no labeling in the cell body layers. Five CCD dogs did, however, exhibit immunoreactivity in layers composed of neuronal dendritic and axonal processes including the stratum moleculare and stratum radiatum [Figures 3F and S5A,B (Supporting File 1)]. P-tau labeling was also regularly observed in the hilus but not stratum granulosum of the dentate gyrus [Figures 3G and S5C (Supporting File 1)]. The strongest immunoreactivity in the hippocampal formation of CCD brains was observed in the white matter pathways of the alveus and fimbria (Figure 3D,E), with labeling of cell processes in transverse or longitudinal cross-section denoted by punctate or thread-like patterns, respectively. This labeling became stronger in the medial portions of the fimbria (Figure S5D, Supporting File 1), with some non-CCD dogs also exhibiting light immunoreactivity in this portion of the hippocampal formation only (Figure S7E, Supporting File 1).

Strong immunoreactivity in the entorhinal cortex was rarely observed, though deeper portions of the cortex exhibited some positivity (Figure 3H), which became stronger still in the subcortical white matter (Figure 3I).

Table 3. Semi-quantitative p-tau S396 pathological severity scoring

	CCD dogs						Non-CCD dogs					
	1	2	3	4	5	6	7	8	9	10	11	12
Hippocampal formation												
Fimbria	+++	++	−	+	++	−	−	−	++	+	−	+
Alveus	++	++	−	+	++	−	−	−	++	+	−	−
Stratum pyramidale (CA1)	−	−	−	−	+	−	−	−	−	−	−	−
Stratum moleculare	+	+	+	−	++	+	−	−	+	−	−	−
Dentate gyrus hilus	+	+	−	+	+	+	−	−	+	−	−	−
Subiculum	+	−	−	−	+	+	−	−	+	−	−	−
EC GM	+	−	+	+	+	−	−	−	+	−	−	−
EC WM	++	+	+	+	++	++	−	−	+	−	−	−
Thalamus and adjacent structures												
Dorsal/ant. thalamic peduncle	++++	+++	+++	+++	+++	++++	++	+	++	−	−	−
Fornix (body)	+++	++	+++	+++	N/A	N/A	N/A	−	N/A	−	−	−
Internal medullary lamina	+++	++	+	+++	+++	++	++	−	++	−	−	−
Anterior nuclear group	++	++	+	+++	++	+++	+	−	−	−	−	−
Stria terminalis	++++	++	++	++++	+++	++++	++	+	+++	+	+	++
Mediodorsal nucleus	+++	+++	++	++	++	++	++	−	++	−	−	−
Stria medullaris thalami	++++	+++	+++	++	+++	++++	++	+	+++	−	−	+
External medullary lamina	++	+	+++	++	++	++	+	−	++	−	−	−
Mammillothalamic tract	+++	++	++	++	+++	++	++	−	++	−	−	−
Mammillary bodies	++	+	+	+	++	+	+	+	−	−	−	−
Neocortical regions												
Temporal cortex	+	+	++	+	−	++	−	−	+	−	−	−
Temporal white matter	++++	+++	++++	++	+	++++	++	+	++	−	−	+
Frontal cortex	+	−	+	+	+	+	−	−	−	−	−	−
Frontal white matter	++	+++	++	+++	++	++	+	−	++	−	−	−
Occipital cortex	+	−	+	+	+	−	−	−	−	−	−	−
Occipital white matter	++	++	+++	+++	++	++	+	−	−	−	−	−
Cingulate cortex	+	+	++	+	+	+	−	−	−	−	−	−
Cingulate white matter	++++	++++	+++	+++	+++	+++	+	+	+	−	−	−
Other structures												
Internal capsule	++++	+	+++	+++	++	++	−	−	+	−	−	−
Cerebellum	−	−	−	−	−	−	−	−	−	−	−	−

S396$^+$ Pathology visualized with EnVision™ labeling was semiquantitatively scored across various substructures in different brain regions. "−" = No labeling. "+" = Light labeling only in limited areas, some punctate immunoreactivity. "++" = More extensive, stronger labeling, lots of immunoreactive puncta. "+++" = Strong labeling over much of tissue region, strong nuclear associated immunoreactivity, small accumulations present. "++++" = Very strong, dense labeling across most of the tissue region, extensive nuclei associated immunoreactivity, lots of accumulations present. An extended version of the table is available in Supporting File 1, as are exemplar images of semiquantitative intensity levels (Figure S2, Supporting File 1). N/A = not available.

Quantitative analysis revealed that the lower intensity S396$^+$ labeling (Cerebellum: $P = 0.0121$; non-CCD Control: $P = 0.0065$), but not the more intense thresholds of accumulated tau (Cerebellum: p> 0.6418; non-CCD Control: $P = 0.5057$) was significantly greater in CCD hippocampi compared to its cerebellum and compared to the hippocampi of non-CCD dogs, respectively (Figure 2C,E). Images from control sections (Figure S6A-C) and control brains (Figure S7D-F′) can be found in Supporting File 1.

S396 p-tau labeling predominates in early stage AD cortical areas and heavily involves subcortical white matter

Within the cortex, accumulations of S396$^+$ p-tau in the neuronal soma were observed more frequently in the temporal (Figure 4B, Figure S6H-I for control slides) and cingulate cortices (Figure 4D) compared to other cortical regions, often with teardrop shape typical of NFTs (Figure 4B,D,F). These were not typically observed in the occipital cortex of any dog (Figure 4H). Generally, immunoreactivity in gray matter was localized to dendrites and axons as evident by radial streaks of immunoreactivity orientated orthogonal to the cortical layers.

The strongest immunoreactivity was in the subcortical white matter, where labeling indicated localization in neuronal axons and glial cell bodies (Figure 4A,C,E,G). This generally became stronger and intra-axonal high-intensity accumulations became more frequent deeper in the white matter (Figure S5O, Supporting File 1).

Quantitatively, while all neocortical regions examined in CCD dogs exhibited significantly greater S396$^+$ labeling compared to healthy controls at lower intensities (Cingulate: $P < 0.0001$;

Temporal: $P = 0.0002$; Frontal: $P = 0.0005$; Occipital: $P = 0.0005$) (Figure 2C), at higher intensity thresholds, only the temporal and cingulate lobes displayed significantly greater levels compared to controls (Cingulate: $P = 0.0011$; Temporal: $P = 0.017$; Frontal: $P = 0.5057$; Occipital: $P = 0.5057$), and compared to the other cortical regions (Cingulate vs. Frontal: $P = 0.0046$, vs. Occipital: $P = 0.0047$; Temporal vs. Frontal: $P = 0.0378$, vs. Occipital: $P = 0.0378$) and hippocampus (Cingulate: $P = 0.0047$; Temporal: $P = 0.0378$) [Figures 2E and S4B (Supporting File 1)]. These differences appear largely because of higher levels in the subcortical white matter, evident in lower magnification micrographs (Figure S5M-U, Supporting

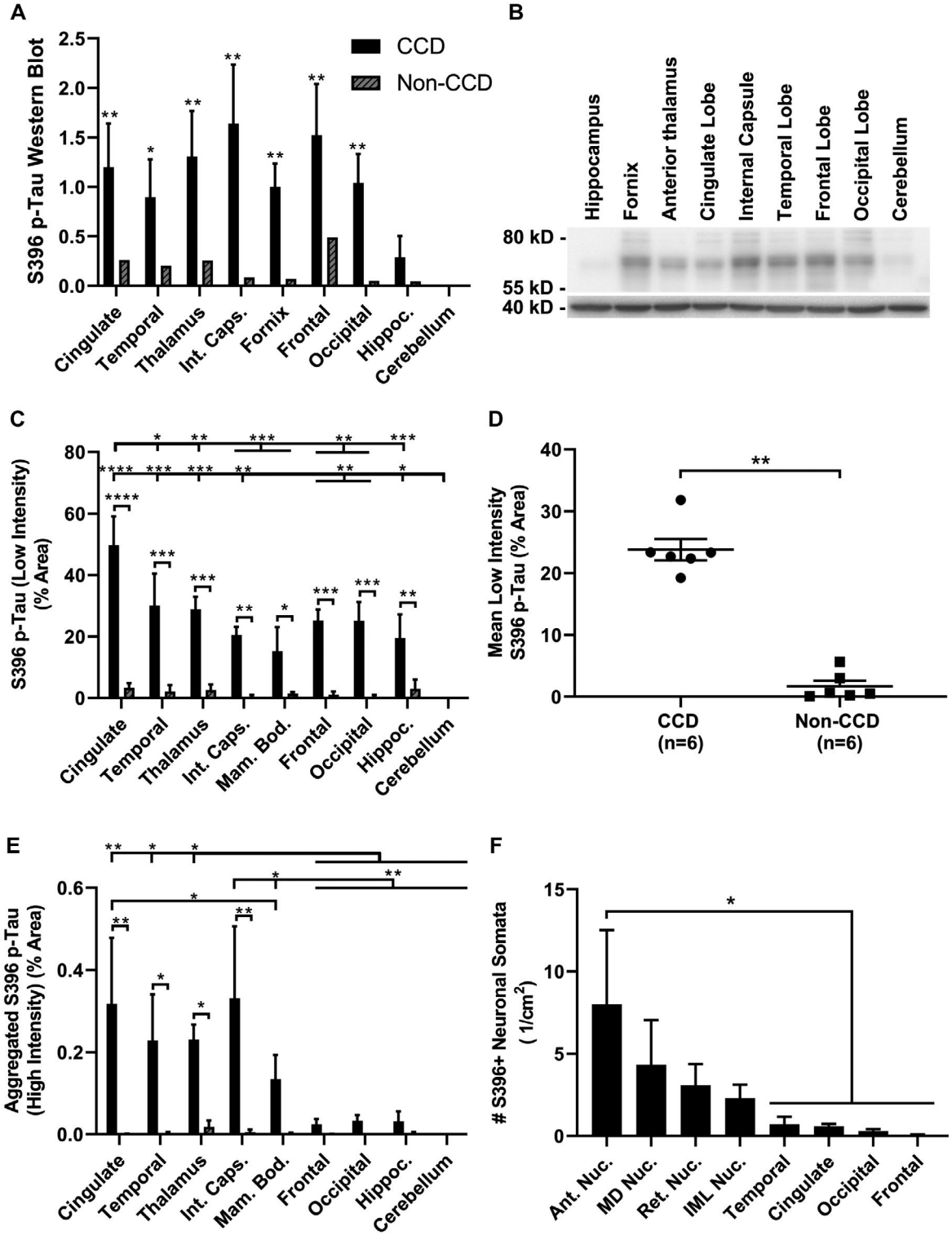

Figure 2. Quantification of S396$^+$ p-tau in CCD dog brain regions. S396 p-tau pathological severity was quantified in different regions in CCD and non-CCD brains by **(A,B)** western blotting and **(C-E)** automated image analysis of EnVision™ labeling at different intensity thresholds, and **(F)** manual counting of EnVision™ labeled sections. **A.** Densitometry of mean relative western blot immunolabeling intensity for different regions in CCD dogs (n = 6) and a non-CCD dog (n = 1). Results of a one-way ANOVA comparing CCD brain regions to the cerebellum is shown. **B.** Western blot of S396 p-tau in a CCD dog, showing main bands between 110 and 55 kD, and β-actin (exposed independently) as a loading control at 42 kD. **(C,E)** Quantification of tissue area labeled at a **(C)** low and **(E)** high intensity threshold by automated image analysis of EnVision™ labeling. Results of two-way ANOVAs comparing all regions within CCD dogs (n = 6) and non-CCD dogs (n = 6) and comparing between groups for each region are shown. **(E)** Mean area labeled at low intensity threshold across regions of CCD dogs compared to non-CCD dogs. Results of a two-tailed Wilcoxon signed-rank test are shown ($P = 0.0078$). **(F)** Manually counted number of S396$^+$ deposits in neuronal somata in different cortices or thalamic nuclei, with results of a one-way ANOVA comparing all regions shown ($P = 0.0283$). All graphs show mean ± SEM, and all statistical analyses were corrected for multiple comparisons using the FDR method. Full statistical results with corrected and uncorrected p values, t values, degrees of freedom, and Cohen's D are available in Supporting Information. $****P < 0.0001$, $***P < 0.001$, $**P < 0.01$, $*P < 0.05$ (Int. Caps = Internal Capsule; Hippoc. = Hippocampus; Mam. Bod = Mammillary Body; Ant. Nuc. = Anterior Thalamic Nucleus; MD Nuc. = Mediodorsal Thalamic Nucleus; Ret. Nuc. = Reticular Nucleus of the Thalamus; IML Nuc. = Nuclei of the Internal Medullary Lamina of the Thalamus).

File 1). Control dogs rarely exhibited immunoreactivity in cortical gray or white matter (Figure S7G-I′, Supporting File 1). No labeling was observed in the cerebellum of any dog (Figure S6J-O, Supporting File 1).

Strongest S396 p-tau in thalamus and internal capsule

A complex but consistent pattern of labeling was observed in nuclei of the thalamus, associated white matter pathways, and other adjacent diencephalic regions of the CCD dogs [Figures 5, S6D-G and S7A-C′ (Supporting File 1) for controls]. Limbic nuclei of the thalamus, most notably the mediodorsal nucleus (Figures 5A and S5I) and anterior nuclear group (Figures 5B and S5F), consistently exhibited strong immunoreactivity, with relatively frequent accumulations of S396 p-tau in neuronal somata. The anterior nuclei contained significantly more S396$^+$ neuronal somata than any cortical region (Figure 2F). By contrast, the ventroanterior nucleus was largely spared (Figure S5K, Supporting File 1), with only light labeling associated with the white matter fascicles. However, the internal medullary lamina (Figures 5G and S5J) and nuclei, external medullary lamina and reticular nucleus (Figure 5H) also featured S396$^+$ accumulations in neuronal somata and axons.

Similar S396$^+$ puncta associated with cross-sectioned axons were evident within white matter fascicles of the mammillothalamic tract (Figures 5I and S5H) and fornix (Figure 5J) across all CCD dogs. The neuronal cell bodies within the gray matter of the mammillary bodies themselves, however, exhibited little immunoreactivity in the dogs (Figure 5K).

The internal capsule also regularly displayed strong S396 labeling in white matter fascicles (Figures 5I and S5L), with large intra-axonal deposits notable in the pathways between the internal capsule and anterior thalamic nuclei in the dorsal thalamic peduncle (Figures 5D and S5G). S396 positivity around glial nuclei was also the commonplace throughout the internal capsule. Two other white matter pathways adjacent to the thalamus, the stria terminalis (Figures 5E and S5G) and stria medullaris (Figure 5F), both exhibited some of the strongest immunoreactivity across the CCD dogs. These two structures were labeled in some non-CCD dogs as well, even in the absence of any other diencephalic immunoreactivity (Figure S7B, Supporting File 1). Two control dogs also exhibited light positivity in other thalamic structures (Figure S7A, Supporting File 1).

Quantitatively, there was significantly more S396$^+$ tauopathy in the thalamus ($P = 0.0003$) and internal capsule ($P = 0.0021$) than in controls, and in particular, these regions had significantly more abnormal accumulations of intensely immunolabeled S396$^+$ p-tau than not only healthy controls (Thalamus: $P = 0.0186$; Internal Capsule: $P = 0.0011$) but also other regions within CCD brains (Thalamus vs. Frontal/ Occipital/ Hippocampus: $P = 0.0378$; Internal Capsule vs. Frontal/ Occipital/ Hippocampus: $P = 0.0046$) (Figure 2C,E). Moreover, of all the regions with elevated high-intensity S396$^+$ p-tau labeling compared to healthy controls (including the cingulate lobe, temporal lobe, and internal capsule), the thalamus clearly exhibited the strongest effect size (Cingulate: Cohen's D = 1.2541; Temporal: D = 1.2701; Thalamus: D = 3.4227; Internal Capsule: D = 1.1783) (See Supporting File 2 for full statistical details).

S396$^+$ double immunofluorescence

Double immunofluorescence with S396 p-tau and panels of neuronal and glial cell markers was performed to clarify the intracellular labeling patterns observed from EnVision™ immunohistochemistry.

MBP antibodies (Figure 6A), which mark the myelin sheath around neuronal axons, and B3T (Figure 6B), a neuronal cytoskeletal marker, confirmed that intensely labeled S396$^+$ p-tau accumulations were within axons in the white matter of CCD dogs, often associated with axonal bulging. This was most pronounced in the internal capsule and deep subcortical white matter. Double labeling was also used to visualize the intraneuronal somata accumulations of S396$^+$ p-tau most frequently observed in the thalamus. S396$^+$ accumulations colocalized with B3T$^+$ neuronal cell bodies and processes, and frequently extended into the axon initial segment and proximal dendrites (Figure 6C). In some sections, S396$^+$ labeling was observed extending over 40 μm into a primary process, and axonal tortuosity could be observed. Three-dimensional (3D) projections from z-stacks are also available in Supporting File 3.

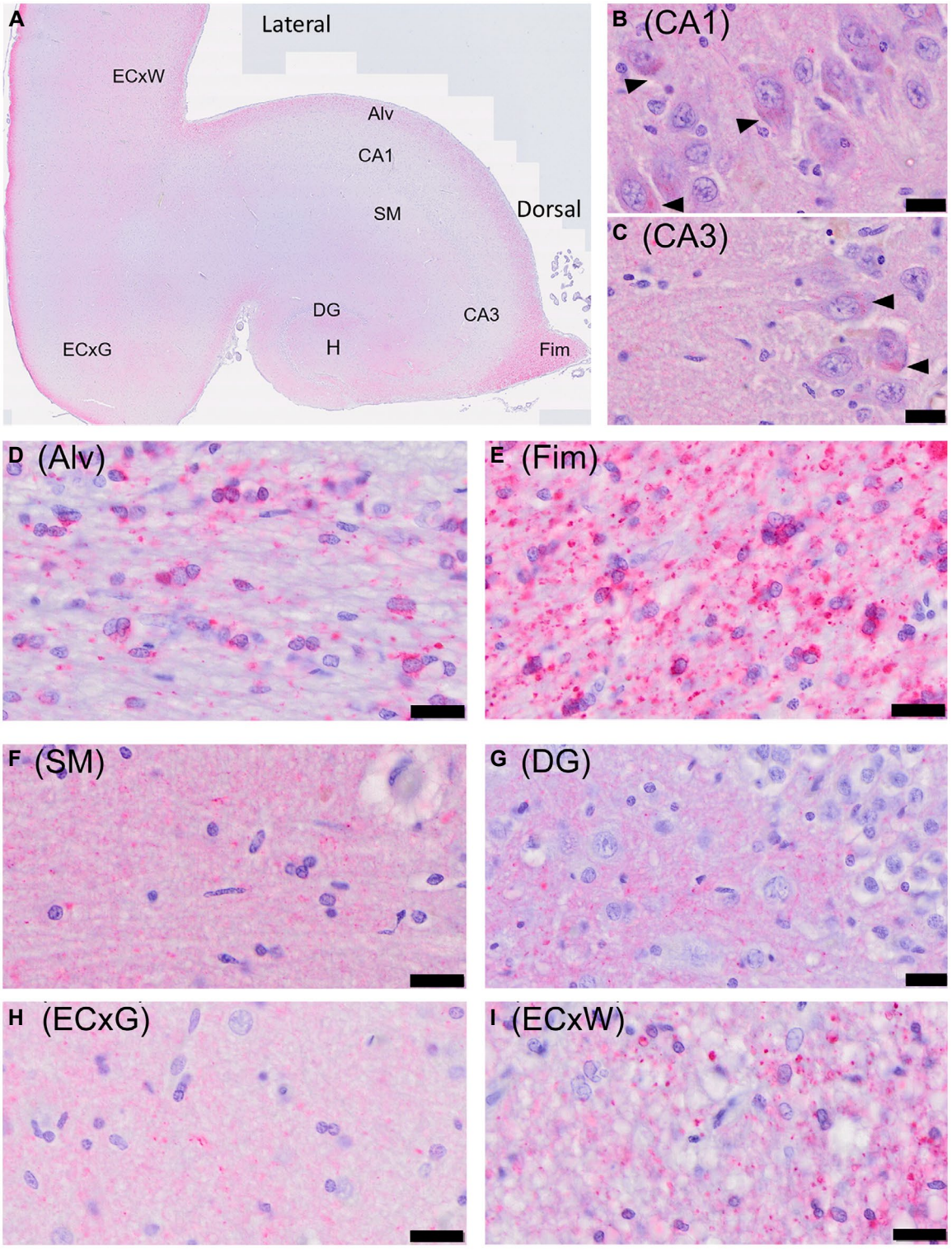

To confirm the nature of the glial associated S396^{+} labeling, double staining was performed with microglial marker Iba-1 (Figure S8A, Supporting File 1), astrocytic marker GFAP (Figure S8B, Supporting File 1) and oligodendrocyte marker O4 (Figure 6D,E). S396 positivity was confirmed to be associated with oligodendrocyte somata, colocalizing with O4 in thalamic and white matter regions. No colocalization of S396 signal with GFAP or Iba-1 was observed in the CCD dogs.

Figure 3. S396$^+$ p-tau immunoreactivity in the ventral hippocampus was especially in white matter and synaptic layers. **(A)** Whole hippocampal formation including entorhinal cortex. Intraneuronal immunoreactivity (arrowheads), especially around the region of the axon hillock, was observed in **(B)** the CA1 stratum pyramidale, and **(C)** the CA3 stratum pyramidale of Canine 5. In other CCD dogs, the stratum pyramidale displayed little S396 labeling. Immunoreactivity was strongest in **(D)** the alveus, and especially in **(E)** the fimbria. Punctate S396$^+$ labeling was also observed in synaptic layers such as **(F)** the stratum moleculare, and in **(G)** the hilar region of the dentate gyrus (not in the stratum granulosum). Sparse immunoreactivity was observed in **(H)** the entorhinal cortex, never in neuronal somata, though **(I)** the white matter of the entorhinal cortex often displayed some immunoreactivity. Sections labeled for S396$^+$ p-tau using EnVision™ labeling and counterstained with hematoxylin. Scale bar represents 20 μm. ECxW = Entorhinal Cortex White Matter, ECxG = Entorhinal Cortex Gray Matter, Alv = Alveus, SM = Stratum Moleculare, DG = Dentate Gyrus, H = Hilus, Fim = Fimbria. Further low magnification micrographs are available in Figure S5A-D, and negative control images are available in Supporting Figures S6A-C and S7D-F (Supporting File 1). [Colour figure can be viewed at wileyonlinelibrary.com]

DISCUSSION

This study set out to investigate tauopathy in community dogs with CCD. Tau is normally confined to the axonal domain, with hyperphosphorylation and redistribution to the somatodendritic compartment abnormal and reflective of an underlying pathology. AT8$^+$ neuronal somata were only observed in one dog, consistent with previous reports that this advanced feature is infrequently observed in CCD brains (40,43). However, we report here that CCD dogs have significantly more S396$^+$ p-tau than non-CCD dogs across a range of brain regions. The regional distribution of this increased S396$^+$ immunoreactivity is reminiscent of patterns described by Braak staging for human AD, and particularly involves structures of the Papez circuit, thought to be heavily implicated in the early stages of the disease (3). Localization in dendrites and white matter axons of the brain further corresponds with early stages of human AD tau dysfunction. On the other hand, we also observed S396 immunoreactivity in oligodendrocytes, a pattern not commonly associated with AD. Together, these data suggest CCD dogs naturally exhibit mixed involvement of AD tau dysfunction with other distinct tau pathological mechanisms.

Absence of AT8 pathology

In the CCD dogs examined in this study, only one dog displayed AT8$^+$ immunoreactivity. These AT8$^+$ neurons were found adjacent to the entorhinal cortex in the composite gyrus of the inferior temporal lobe (52). All AT8$^+$ neurons were in superficial cortical layers, which closely correspond to observations from Braak and Braak (10), regarding Stage I tauopathy in AD patients. Given the close association between CCD and age (36), it is perhaps not coincidental that this was also the oldest dog in the group.

The absence of AT8$^+$ tau in CCD dogs, especially given the abundance of S396 p-tau, may be because of several factors. Phosphorylation of the tau protein can occur at many different amino acid residues. It is plausible that canine tau in CCD is phosphorylated at different residues to human tau in AD, and that the AT8 antibody, specific to S202 and T205 phospho-epitopes, may not represent an ideal marker for canine NFTs. Perhaps more likely, as many previous authors have also suggested, it may simply be because CCD dogs do not live long enough for the tauopathy to progress to the NFT stage (16,40). Behavioral changes central to CCD such as spontaneous aggression and nocturnal disturbances are poorly tolerated in community dogs, with euthanasia typically considered within a short time frame following manifestation of these symptoms.

Intense abnormal S396 p-tau

Quantification of S396 immunohistochemistry was supported by western blotting and revealed that all regions examined in CCD brains, except the cerebellum, had significantly more S396$^+$ immunoreactivity than non-CCD controls. This agrees with a previous study utilizing western blotting, which reported a higher level of S396 p-tau in the dorsal hippocampus and parietal cortex of CCD dogs (57). When thresholding for the most intense immunoreactivity, only the thalamus, temporal and cingulate cortices and internal capsule had significantly higher levels of S396 p-tau immunoreactivity than other regions, potentially indicative of a more advanced stage of tau dysfunction or pathology. This cortical and thalamic distribution is reminiscent of early stage human AD, where higher levels of NFTs are observed here than in the frontal and occipital cortices (8,10). However, while we observed evidence for abnormal re-distribution to the neuronal soma and hyperphosphorylation of tau, we did not observe evidence of tau aggregation in to PHFs and the generation of NFTs in CCD. Given non-fibrillar accumulation of p-tau in the neuronal soma precedes the development of NFTs (5), the overall pattern suggests that tau pathology in dogs is at an even earlier stage than in humans with early stage AD.

In most gray matter structures, S396$^+$ p-tau labeling was largely absent from the neuronal cell bodies. Rather, immunoreactivity was located in dendritic processes and neurites of the neuropil. This pattern aligns with findings from previous studies of CCD pathology (33,57). However, across all regions, positivity was more predominantly observed in white matter axons, supporting findings by Wegiel, Wisniewski and Soltysiak (50) who observed Tau-1$^+$ deposits in the white matter of the canine cortex and hippocampus. Rodent and cellular AD models have shown that S396$^+$ p-tau appears first in the axons and dendrites prior to its aggregation into NFTs within the neuronal soma (17). Although the precise mechanism for NFT formation remains unknown, whether through mislocalization into the soma (17,26,49), or through *de novo* synthesis within the somatodendritic

domain (4,27), the predominance of white matter tauopathy in CCD provides further evidence for the former (53,55). Double immunofluorescence data confirmed the intra-axonal localization of this tau, which was observed to be associated with bulging of the axon in some regions. Studies on nematode and murine tauopathy models neurons have also observed such bulging, likely disrupting intraneuronal trafficking and signaling (25,28).

Nevertheless, neuronal soma accumulation of S396 was also observed in some specific brain regions, most abundantly

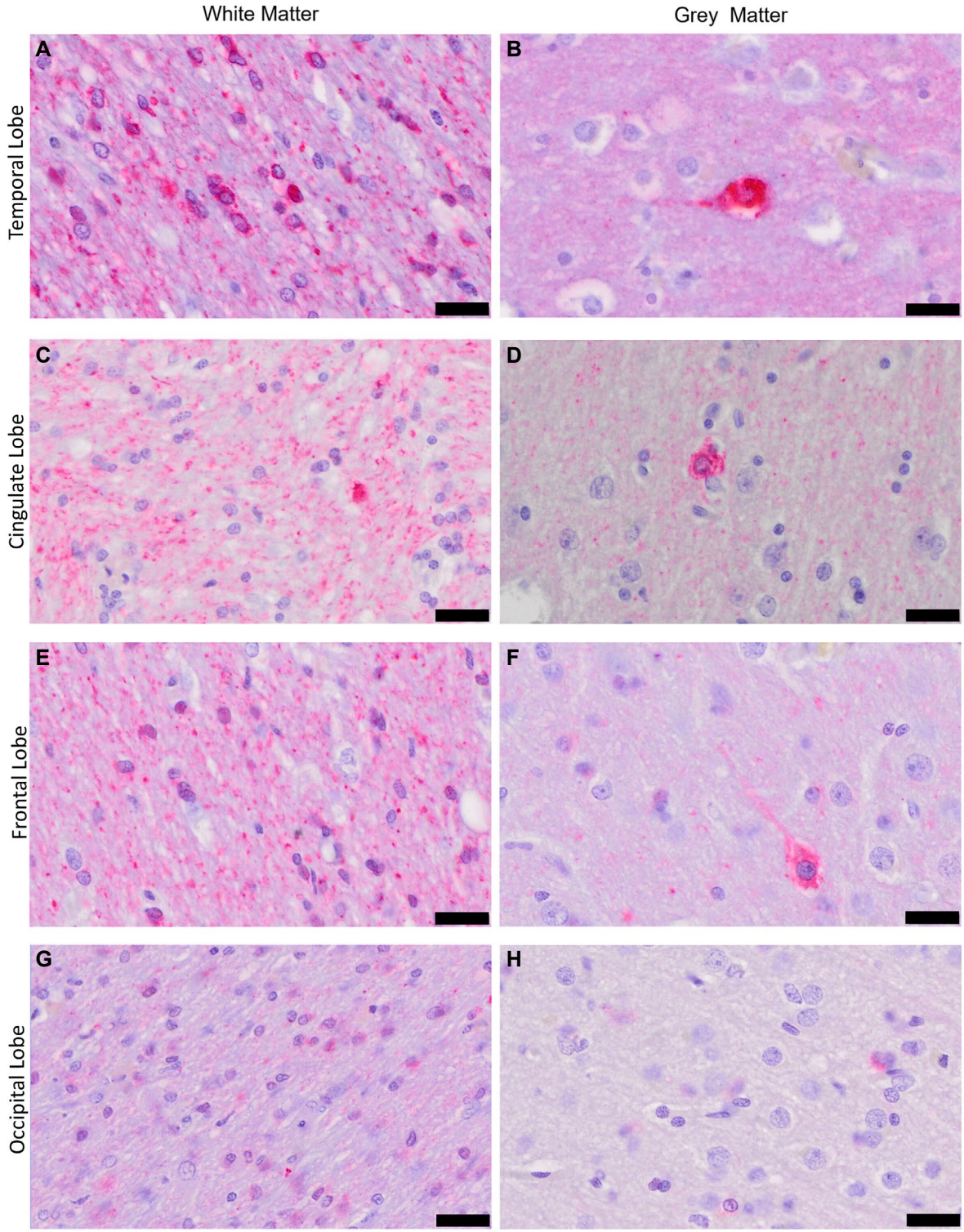

Figure 4. S396$^+$ p-tau immunolabelling was more intense in cortical white matter than gray matter. The first column shows EnVision™ labeling for S396$^+$ p-tau pathology in subcortical white matter compared with cortical gray matter in the right column for **(A,B)** the temporal cortex, where labeling was observed to be most intense, especially in the white matter adjacent to the lateral ventricle, with extensive perinuclear glial labeling, **(C,D)** the cingulate lobe, where strong labeling was also observed in both the cingulum bundle and the cortical gray matter, including intraneuronal labeling in several dogs; **(E,F)** the frontal lobe, where labeling in the gray matter was much more sparse though intraneuronal deposits were occasionally apparent and labeling in deep portions of the white matter was still evident; and **(G,H)** the occipital lobe, where gray matter immunoreactivity was much less strong compared to other cortical regions, though white matter and glial nuclear labeling were still apparent. Sections labeled for S396$^+$ p-tau using EnVision™ labeling and counterstained with hematoxylin. Scale bars represent 20 μm. Further low magnification micrographs are available in Figure S5m-u, and negative control images are available in Figures S6h-o and 7g-i (Supporting File 1). [Colour figure can be viewed at wileyonlinelibrary.com]

in the composite gyrus of the inferior temporal cortex of Canine 3, the oldest animal, who also displayed AT8$^+$ NFT pathology in the same area. This suggests that this intrasomal S396 p-tau may represent a stage closer to NFT formation than the axonal tau changes described above. Furthermore, the inferior temporal and parahippocampal cortices are known to receive strong projections in humans and other mammals from the anterior thalamic nuclei through the cingulum bundle and via the cingulate and retrosplenial cortices (11). When coupled with the theory that p-tau is capable of migrating between brain regions trans-synaptically (44), this provides a potential reason as to why this cortical region is the first to develop AT8$^+$ NFTs.

In the rest of the CCD dogs, however, soma-localized S396$^+$ p-tau was more abundant in the thalamus than any other brain region studied, especially in the anterior nucleus (Figure 2F), one of the earliest structures to display tauopathy in AD (10). The pattern of thalamic S396$^+$ p-tau immunoreactivity we observed as a whole, displayed remarkably close correspondence to that described in AD using labeling for NFT pathology (9,34). For example, the involvement of limbic nuclei contrasted with sparing of motor nuclei, and the description of staining between the anteroventral nucleus and ependymal wall of the third ventricle (9), bear striking resemblance to S396$^+$ labeling in the CCD dogs (Figure 5A). This close correspondence of CCD S396$^+$ p-tau to human neurofibrillary patterns in the thalamus specifically, lends further support for the idea that S396$^+$ p-tau in the neuronal somata of CCD dogs may reflect a stage immediately prior to AT8$^+$/argyrophilic NFT formation. Combined with the greater degree of aggregation of S396$^+$ p-tau in the thalamus and temporal cortex of CCD dogs compared to the occipital and frontal cortices, a favorable comparison to Braak staging of NFT pathology in AD may be drawn.

Despite this, only low levels of tau changes were observed in the neuronal cell bodies of the hippocampus and entorhinal cortex as compared to the thalamus. This is perplexing, given the importance of these structures by traditional accounts of AD tauopathy. Notably, however, hippocampal efferent axonal structures such as the alveus, fimbria and fornix, were all strongly immunoreactive for S396 p-tau. Similarly, specific hippocampal layers containing pyramidal cell dendrites and axonal projections such as the stratum moleculare and stratum radiatum were also immunoreactive. This suggests that neurons in hippocampal circuits are, in fact, affected by tauopathy, but at the earlier stage illustrated in Figure 7B, featuring white matter dysfunction prior to the soma accumulation seen in the thalamus and various cortical regions as per Figure 7C, which seems precursory to the further advanced NFT stage (Figure 7D). As a result of the proportional under-representation of the alveus, fimbria and fornix in the total area of the hippocampal tissue sections, this observation was not reflected in the immunolabeling or western blotting quantification data and as such, the hippocampal neurons should not be considered to be spared of tau dysfunction in the CCD dogs (as per Figure 7A).

The Papez Circuit

The observations of tauopathy in the limbic thalamus and hippocampofugal pathways can also be extended to further limbic circuitry. Papez (31) described a circuit that links the hippocampus and limbic thalamus via the mammillary bodies and cingulate cortex (Figure 7E). The circuit comprises critical structures for episodic memory, which are compromised in AD and contribute to cognitive impairment. The thalamus in particular is implicated as having a major role in the incipience of tauopathy in AD (3), and lesions to the anterior nuclei have been related to spatial memory dysfunction in rodents, a common behavioral deficit in CCD (2). Furthermore, human diffusion tensor imaging has shown disruptions to thalamic connectivity through the fornix, dorsal thalamic peduncle, and stria terminalis are associated with AD (58). Especially relevant here is the finding that degeneration of white matter pathways in the Papez circuit rather than occipital and prefrontal white matter is also associated with AD (1). The Papez circuit-based model for AD is thus particularly relevant and supported by this study, as immunoreactivity was observed along the entire circuit as delineated in Figure 7E. Thus, not only is the evidence of tauopathy in the CCD limbic thalamus consistent with this model, but it may also explain the pathology observed in the cingulate cortex, cingulum bundle and internal capsule through which they are interconnected (51). As such, the hyperphosphorylated tau observed in CCD brains occurs in a series of structures that are not only anatomically connected but functionally relevant to the clinical syndrome.

Glial tauopathy

S396 positivity was frequently observed within oligodendrocytes, especially in the internal capsule, subcortical white

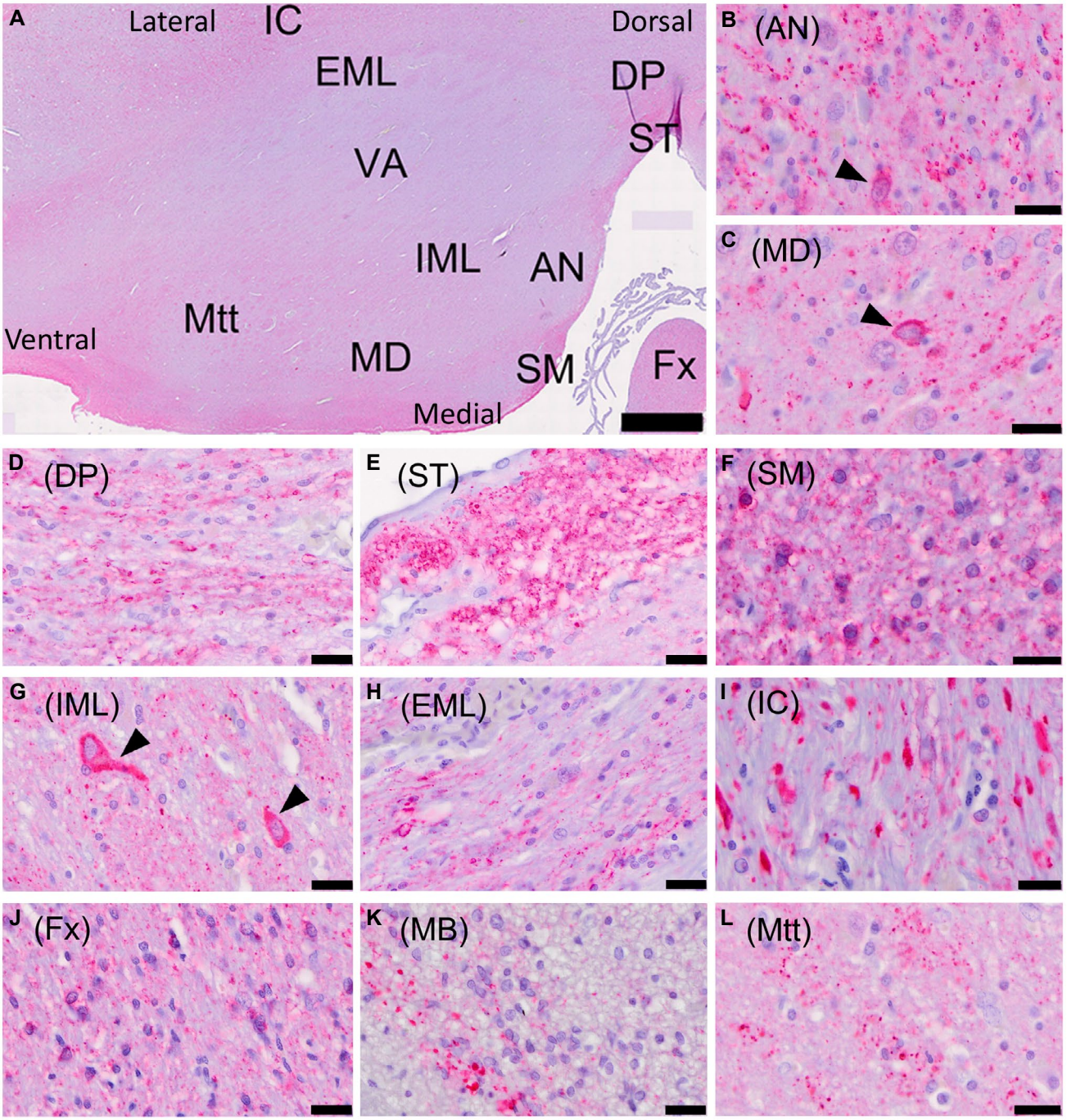

Figure 5. Extensive S396⁺ pathology was observed in the thalamus and adjacent subcortical structures. **A.** Representative image of a section through the anterior thalamus including internal capsule. Labeling was evident in neuronal cell bodies (arrowheads) of **(B)** the anterior thalamic nuclei, and **(C)** the mediodorsal thalamic nucleus, as well as in neuronal neurites and axons in these regions. Labeling in **(D)** the dorsal thalamic peduncle, a white matter pathway leading into the anterior nuclear group, was also especially evident, as was labeling in **(E)** the stria terminalis, and **(F)** the stria medullaris. Immunopositive neuronal cell bodies and neurites were also observed in **(G)** the internal medullary lamina, and **(H)** the external medullary lamina, and their associated nuclei. **I.** The internal capsule displayed large accumulations of labeled material and perinuclear glial labeling was also notable both in this white matter pathway and in **(J)** the fornix. **K.** The mammillary bodies only displayed small amounts of immunoreactivity not associated with neuronal somata, though **(L)** the mammillothalamic tract regularly displayed strong punctate labeling associated with transverse white matter fascicles. Sections labeled for S396⁺ p-tau using EnVision™ labeling and counterstained with hematoxylin. All scale bars represent 20 μm except (a) where scale bar represents 1 mm. IC = internal capsule, EML = external medullary lamina, VA = ventroanterior nucleus, Mtt = mammillothalamic tract, IML = internal medullary lamina, MD = mediodorsal nucleus, DP = dorsal thalamic peduncle, ST = stria terminalis, AN = Anterior Nucleus, SM = stria medullaris, Fx = Fornix. Further low magnification micrographs are available in Figure S5E-L, and negative control images are available in Figures S6D-G and S7A-C (Supporting File 1). [Colour figure can be viewed at wileyonlinelibrary.com]

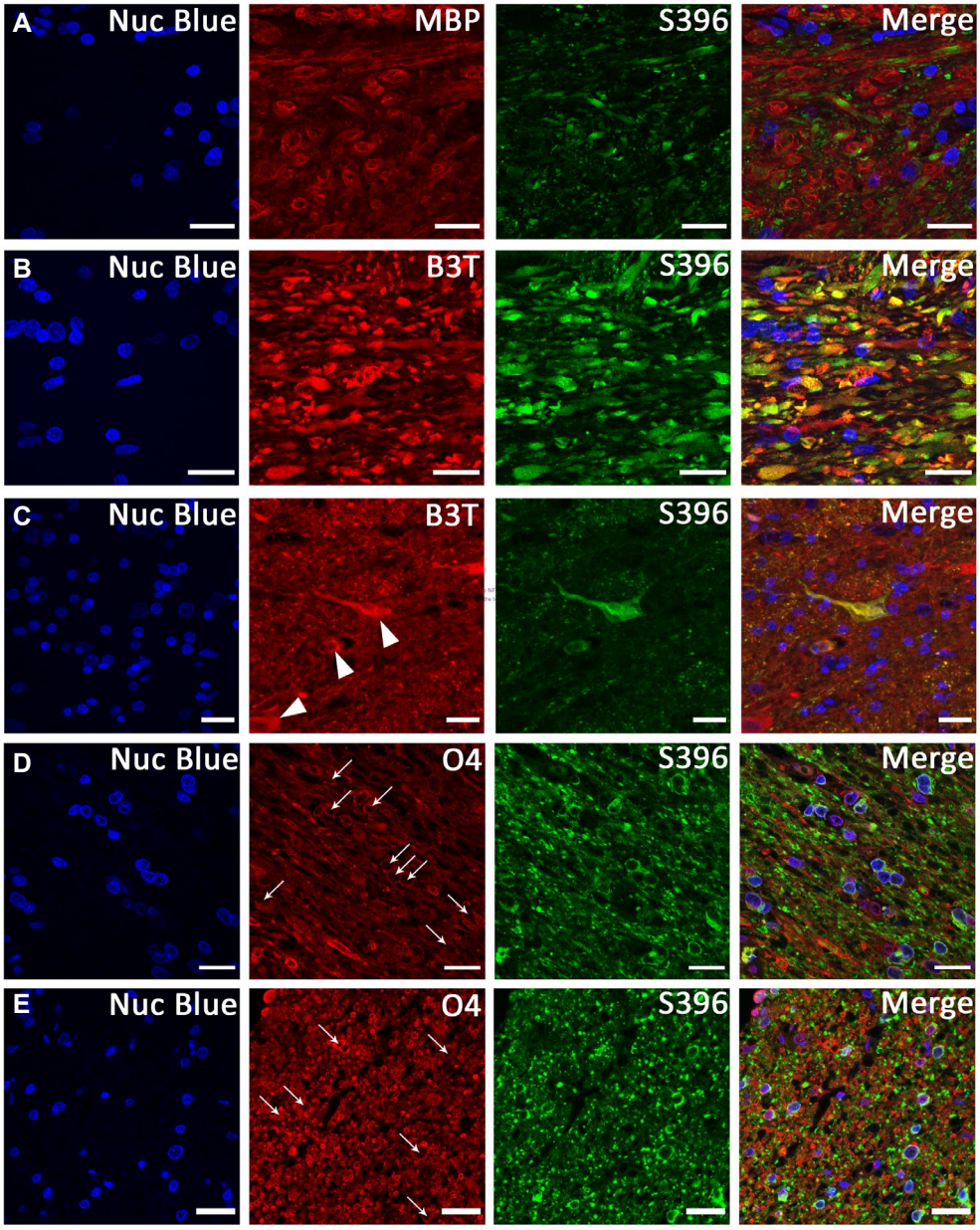

Figure 6. Double immunofluorescence demonstrates S396⁺ p-tau accumulations within white matter axons, neuronal somata and oligodendrocyte somata. **A.** Myelin basic protein (MBP) marking the myelin sheath around axons in the internal capsule, with S396⁺ accumulating within the myelin-marked axons and causing bulges at the sites of accumulation. **B.** B3T neuronal marker demonstrating axons in the internal capsule colocalizing with green S396⁺ accumulations, further demonstrating the presence of tau accumulation within neuronal axons. **C.** Multipolar neuron in the reticular nucleus of the thalamus displaying colocalization of neuronal marker B3T and S396 in the soma and extending into several neurites, with the nucleus laterally displaced. (B3T⁺ cells noted with arrowheads) **(D,E)** Oligodendrocyte marker O4. **C.** S396⁺ accumulations in temporal cortex of white matter, visible within longitudinal axons marked by O4 in red, as well as colocalizing with perinuclear O4. **E,** Stria medullaris, demonstrating axons in cross section (red) containing S396⁺ immunoreactivity within them (green), as well as green S396⁺ colocalizing around nuclei with red O4 oligodendrocyte marker. Arrows mark some S396⁺O4⁺ cells. (**A-C**) are maximum intensity projections of z-stacks (3D projections available in Supporting File 3), (**A,B,D,E**) imaged under 60x objective, (**C**) imaged under 40x objective; scale bar represents 20 μm. [Colour figure can be viewed at wileyonlinelibrary.com]

matter of the temporal lobe (close to the border of the lateral ventricle), cingulum bundle and fimbria/fornix. Similar oligodendrocyte tauopathy (including reports of S396 deposits) is commonly observed in neurodegenerative diseases such as corticobasal degeneration, progressive supranuclear palsy and Pick's disease (24). Boluda, Iba, Zhang, Raible, Lee and Trojanowski (6) also describe similar tau labeling within oligodendrocytes of the fimbria in transgenic mice which

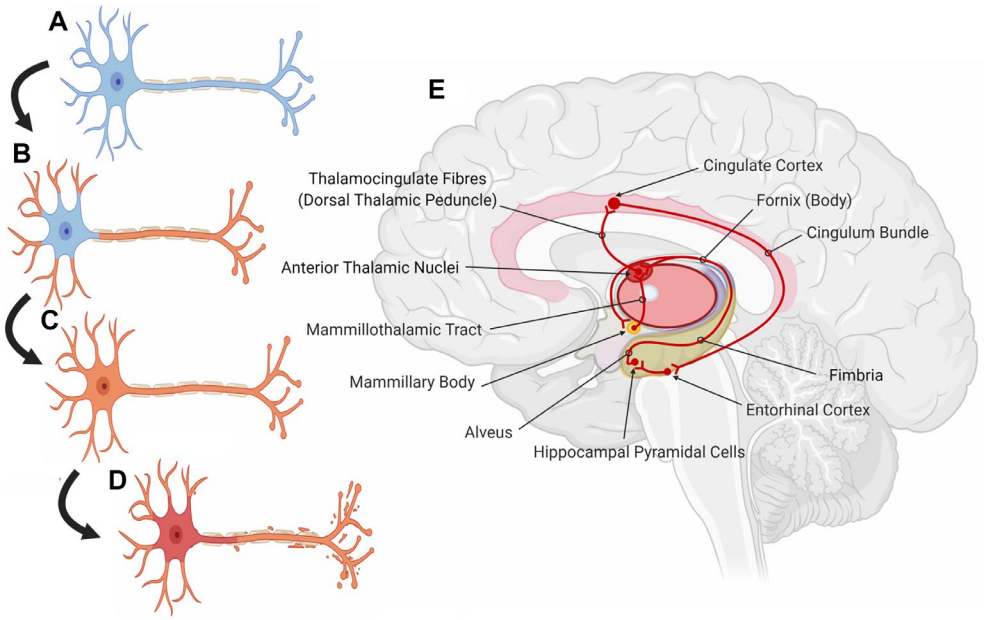

Figure 7. A theoretical model for pathological tau phosphorylation and progression in CCD. **A.** Tau is physiologically found primarily in the axon, where it stabilizes microtubules, as well as in dendrites. **B.** Tau becomes hyperphosphorylated at the S396 residue in the axon, dendrites and axon terminals, and begins accumulating. **C.** P-tau mis-localizes to soma where it begins to accumulate further, likely as a precursor to neurofibrillary pathology. **D.** Mis-localized, misfolded hyperphosphorylated tau in the soma forms fibrillary structures such as paired helical filaments and becomes an AT8^{+} neurofibrillary tangle. **E.** Schema for the Papez Circuit as examined in the present study, overlaid on a human brain. Neurons in CCD brains within this circuit and related brain regions were observed to be at various stages of tau dysfunction illustrated in **B–D**. [Colour figure can be viewed at wileyonlinelibrary.com]

received intracerebral injections of pathological tau from human brains with corticobasal degeneration. The impact of oligodendrocyte tauopathy on myelin sheath integrity is not well understood, but it may play an important role in the dysfunction of neuronal circuitry implicated in CCD-related cognitive decline.

As such, CCD brains reflect a complex mix of tau abnormalities potentially relevant to Alzheimer's disease and other related tauopathies. This is, in fact, also a common observation in human dementia studies, with one recent study demonstrating a admix of pathology to be the most common cause of cognitive impairment, with classical AD pathology rarely existing in isolation (7).

Given the apparent absence of NFT-related neurodegeneration, the pathological mediator of cognitive decline in CCD remains unclear. An increasing number of recent studies posit that oligomeric Aβ or p-tau represent pathological species that may drive cognitive decline through synaptic dysfunction (21,22). Synapse loss is regarded as the closest correlate of cognitive dysfunction (41,45,46), and elevated synapse-related S396 p-tau has been observed in AD mouse models (55) and CCD dogs (43). While we do not confirm whether the S396 + p-tau accumulations observed in our study are oligomeric, this synapse-related tauopathy may correspond to the S396 positivity that we observed within synaptic layers of the hippocampus. The abnormal accumulation of tau within axons and oligodendrocytes may also impede intracellular trafficking and signal transmission, respectively. Examining synaptic density and myelin sheath integrity as early stage pathogenic mechanisms in CCD is an important avenue of future research.

CONCLUSION

This study reveals new insights about tauopathy in the CCD brain. P-tau in regions of early Braak staging, subcellular localization within neuronal axons and dendrites and ubiquitous presence across anatomically relevant circuits, altogether suggest a pattern reminiscent of early stage AD. While we do not investigate amyloid here, plaques and cerebral amyloid angiopathy are well established features of CCD that likely coexist with the tau changes described here as part of a broader, AD-like complex pathological process (15,56). CCD therefore naturally recapitulates many complex aspects of early stage tauopathy as well as other AD pathologies (32,56). Considering continued failures to develop new effective therapies, this preclinical model may be of significant translational value.

ACKNOWLEDGEMENTS

The authors acknowledge the instruments, and scientific and technical assistance of the Sydney Microscopy and Microanalysis team from Microscopy Australia at the University of Sydney, a facility that is funded by the University, and State and Federal Governments. The authors would also like to acknowledge the help of Dr Antony

Harding in the processing of the canine brains, and Dr Michael Lovelace for kindly supplying us with a variety of oligodendrocyte antibodies.

This work was funded by the National Health and Medical Research Council of Australia, a University of Sydney SOAR Fellowship, the Yulgilbar Alzheimer Research Program and generous gifts from the Smith and Jolly families. The authors would also like to acknowledge the scholarship support provided by the University of Sydney, in particular from the Discipline of Anatomy and Histology. These bodies had no role in the design of the study, collection, analysis, and interpretation of data or in writing the manuscript.

CONFLICT OF INTEREST

The authors declare no conflicts of interest. MV is scientific founder of Skin2Neuron Pty Ltd (S2N), in which he and TD have a financial interest. S2N did not fund or have any role in this work.

AUTHOR'S CONTRIBUTIONS

Conceptualization: Ajantha Abey, Claire Goldsbury, Thomas Duncan, Michael Valenzuela; Methodology: All Authors; Tissue Acquisition and preparation: Michael Buckland, Thomas Duncan, Ajantha Abey; Formal analysis and investigation: Ajantha Abey, Danielle Davis; Writing: Ajantha Abey; Review and editing: All Authors.

ETHICS APPROVAL AND CONSENT TO PARTICIPATE

All procedures described herein were conducted according to NSW and Australian Law.

DATA AVAILABILITY STATEMENT

The datasets used and analyzed during the current study available from the corresponding author on reasonable request. Some additional data including images and further statistical data are including in Supporting files.

REFERENCES

1. Acosta-Cabronero J, Williams GB, Pengas G, Nestor PJ (2009) Absolute diffusivities define the landscape of white matter degeneration in Alzheimer's disease. *Brain* **133**:529–539. https://doi.org/10.1093/brain/awp257.
2. Aggleton JP, Nelson AJD (2015) Why do lesions in the rodent anterior thalamic nuclei cause such severe spatial deficits? *Neurosci Biobehav Rev* **54**:131–144. https://doi.org/10.1016/j.neubiorev.2014.08.013.
3. Aggleton JP, Pralus A, Nelson AJD, Hornberger M (2016) Thalamic pathology and memory loss in early Alzheimer's disease: moving the focus from the medial temporal lobe to Papez circuit. *Brain* **139**:1877–1890. https://doi.org/10.1093/brain/aww083.
4. Amar F, Sherman MA, Rush T, Larson M, Boyle G, Chang L *et al* (2017) The amyloid-beta oligomer A beta*56 induces specific alterations in neuronal signaling that lead to tau phosphorylation and aggregation. *Sci Signal* **10**:14. https://doi.org/10.1126/scisignal.aal2021.
5. Augustinack JC, Schneider A, Mandelkow E-M, Hyman BT (2002) Specific tau phosphorylation sites correlate with severity of neuronal cytopathology in Alzheimer's disease. *Acta Neuropathol* **103**:26–35. https://doi.org/10.1007/s00401010100423.
6. Boluda S, Iba M, Zhang B, Raible KM, Lee VMY, Trojanowski JQ (2015) Differential induction and spread of tau pathology in young PS19 tau transgenic mice following intracerebral injections of pathological tau from Alzheimer's disease or corticobasal degeneration brains. *Acta Neuropathol* **129**:221–237. https://doi.org/10.1007/s00401-014-1373-0.
7. Boyle PA, Yu L, Wilson RS, Leurgans SE, Schneider JA, Bennett DA (2018) Person-specific contribution of neuropathologies to cognitive loss in old age. *Ann Neurol* **83**:74–83. https://doi.org/10.1002/ana.25123.
8. Braak H, Alafuzoff I, Arzberger T, Kretzschmar H, Del Tredici K (2006) Staging of Alzheimer disease-associated neurofibrillary pathology using paraffin sections and immunocytochemistry. *Acta Neuropathol* **112**:389–404. https://doi.org/10.1007/s00401-006-0127-z.
9. Braak H, Braak E (1991) Alzheimer's disease affects limbic nuclei of the thalamus. *Acta Neuropathol* **81**:261–268. https://doi.org/10.1007/BF00305867.
10. Braak H, Braak E (1991) Neuropathological staging of Alzheimer-related changes. *Acta Neuropathol* **82**:239–259. https://doi.org/10.1007/bf00308809.
11. Bubb EJ, Metzler-Baddeley C, Aggleton JP (2018) The cingulum bundle: anatomy, function, and dysfunction. *Neurosci Biobehav Rev* **92**:104–127. https://doi.org/10.1016/j.neubiorev.2018.05.008.
12. Cummings BJ, Head E, Afagh AJ, Milgram NW, Cotman CW (1996) beta-amyloid accumulation correlates with cognitive dysfunction in the aged canine. *Neurobiol Learn Mem* **66**:11–23. https://doi.org/10.1006/nlme.1996.0039.
13. Cummings BJ, Head E, Ruehl W, Milgram NW, Cotman CW (1996) The canine as an animal model of human aging and dementia. *Neurobiol Aging* **17**:259–268. https://doi.org/10.1016/0197-4580(95)02060-8.
14. Dai C-L, Hu W, Tung YC, Liu F, Gong C-X, Iqbal K (2018) Tau passive immunization blocks seeding and spread of Alzheimer hyperphosphorylated Tau-induced pathology in 3 × Tg-AD mice. *Alzheimers Res Ther* **10**:13. https://doi.org/10.1186/s13195-018-0341-7.
15. Dewey CW, Davies ES, Xie H, Wakshlag JJ (2019) Canine Cognitive dysfunction: pathophysiology, diagnosis, and treatment. *Vet Clin North Am Small Anim Pract* **49**:477–499. https://doi.org/10.1016/j.cvsm.2019.01.013.
16. Dimakopoulos AC, Mayer RJ (1579S) Aspects of neurodegeneration in the canine brain. *J Nutr* **132**:1579S–1582S.
17. Foidl BM, Humpel C (2018) Differential hyperphosphorylation of Tau-S199, -T231 and -S396 in organotypic brain slices of Alzheimer mice. A model to study early tau hyperphosphorylation using okadaic acid. *Front Aging Neurosci* **10**. https://doi.org/10.3389/fnagi.2018.00113.
18. Gong CX, Iqbal K (2008) Hyperphosphorylation of microtubule-associated protein tau: a promising therapeutic target for Alzheimer disease. *Curr Med Chem* **15**:2321–2328.
19. Head E (2011) Neurobiology of the aging dog. *Age* **33**:485–496. https://doi.org/10.1007/s11357-010-9183-3.

20. Head E, McCleary R, Hahn FF, Milgram NW, Cotman CW (2000) Region-specific age at onset of beta-amyloid in dogs. *Neurobiol Aging* **21**:89–96. https://doi.org/10.1016/s0197-4580(00)00093-2.
21. Hong S, Beja-Glasser VF, Nfonoyim BM, Frouin A, Li S, Ramakrishnan S *et al* (2016) Complement and microglia mediate early synapse loss in Alzheimer mouse models. *Science* **352**:712–716.
22. Huang YP, Wu ZZ, Zhou B (2016) Behind the curtain of tauopathy: a show of multiple players orchestrating tau toxicity. *Cell Mol Life Sci* **73**:1–21. https://doi.org/10.1007/s00018-015-2042-8.
23. Iqbal K, Gong C-X, Liu F (2013) Hyperphosphorylation-induced tau oligomers. *Front Neurol* **4**:112. https://doi.org/10.3389/fneur.2013.00112.
24. Iwatsubo T, Hasegawa M, Ihara Y (1994) Neuronal and glial tau-positive inclusions in diverse neurologic diseases share common phosphorylation characteristics. *Acta Neuropathol* **88**:129–136. https://doi.org/10.1007/BF00294505.
25. Kraemer BC, Zhang B, Leverenz JB, Thomas JH, Trojanowski JQ, Schellenberg GD (2003) Neurodegeneration and defective neurotransmission in a *Caenorhabditis elegans* model of tauopathy. *Proc Natl Acad Sci U S A* **100**:9980–9985. https://doi.org/10.1073/pnas.1533448100.
26. Lee VMY, Goedert M, Trojanowski JQ (2001) Neurodegenerative Tauopathies. *Annu Rev Neurosci* **24**:1121–1159. https://doi.org/10.1146/annurev.neuro.24.1.1121.
27. Li CZ, Gotz J (2017) Somatodendritic accumulation of Tau in Alzheimer's disease is promoted by Fyn-mediated local protein translation. *Embo J* **36**:3120–3138. https://doi.org/10.15252/embj.201797724.
28. Lin WL, Lewis J, Yen SH, Hutton M, Dickson DW (2003) Ultrastructural neuronal pathology in transgenic mice expressing mutant (P301L) human tau. *J Neurocytol* **32**:1091–1105. https://doi.org/10.1023/b:Neur.0000021904.61387.95.
29. Lowe A, Dalton M, Sidhu K, Sachdev P, Reynolds B, Valenzuela M (2015) Neurogenesis and precursor cell differences in the dorsal and ventral adult canine hippocampus. *Neurosci Lett* **593**:107–113. https://doi.org/10.1016/j.neulet.2015.03.017.
30. Mondragón-Rodríguez S, Perry G, Luna-Muñoz J, Acevedo-Aquino MC, Williams S (2013) Phosphorylation of tau protein at sites Ser396–404 is one of the earliest events in Alzheimer's disease and Down syndrome. *Neuropathol Appl Neurobiol* **40**:121–135. https://doi.org/10.1111/nan.12084.
31. Papez JW (1937) A proposed mechanism of emotion. *Arch Neurol Psychiat* **38**:725–743. https://doi.org/10.1001/archneurpsyc.1937.02260220069003.
32. Prpar Mihevc S, Majdič G (2019) Canine cognitive dysfunction and alzheimer's disease – two facets of the same disease? *Front Neurosci* **13**:604. https://doi.org/10.3389/fnins.2019.00604.
33. Pugliese M, Mascort J, Mahy N, Ferrer I (2006) Diffuse beta-amyloid plaques and hyperphosphorylated tau are unrelated processes in aged dogs with behavioral deficits. *Acta Neuropathol* **112**:175–183. https://doi.org/10.1007/s00401-006-0087-3.
34. Rub U, Stratmann K, Heinsen H, Del Turco D, Ghebremedhin E, Seidel K *et al* (2016) Hierarchical distribution of the tau cytoskeletal pathology in the thalamus of Alzheimer's disease patients. *J Alzheimers Dis* **49**:905–915. https://doi.org/10.3233/jad-150639.
35. Sabattini E, Bisgaard K, Ascani S, Poggi S, Piccioli M, Ceccarelli C *et al* The EnVision++ system: a new immunohistochemical method for diagnostics and research. Critical comparison with the APAAP, ChemMate, CSA, LABC, and SABC techniques. *J Clin Pathol* 1998;**51**:506. https://doi.org/10.1136/jcp.51.7.506
36. Salvin HE, McGreevy PD, Sachdev PS, Valenzuela MJ (2010) Under diagnosis of canine cognitive dysfunction: a cross-sectional survey of older companion dogs. *Vet J* **184**:277–281. https://doi.org/10.1016/j.tvjl.2009.11.007.
37. Salvin HE, McGreevy PD, Sachdev PS, Valenzuela MJ (2011) The canine cognitive dysfunction rating scale (CCDR): a data-driven and ecologically relevant assessment tool. *Vet J* **188**:331–336. https://doi.org/10.1016/j.tvjl.2010.05.014.
38. Sankaranarayanan S, Barten DM, Vana L, Devidze N, Yang L, Cadelina G *et al* (2015) Passive immunization with phospho-tau antibodies reduces tau pathology and functional deficits in two distinct mouse tauopathy models. *PLoS One* **10**:e0125614. https://doi.org/10.1371/journal.pone.0125614.
39. Schindelin J, Arganda-Carreras I, Frise E, Kaynig V, Longair M, Pietzsch T *et al* (2012) Fiji: an open-source platform for biological-image analysis. *Nat Methods* **9**:676–682. https://doi.org/10.1038/nmeth.2019.
40. Schmidt F, Boltze J, Jager C, Hofmann S, Willems N, Seeger J *et al* (2015) Detection and quantification of beta-amyloid, pyroglutamyl a beta, and tau in aged canines. *J Neuropathol Exp Neurol* **74**:912–923. https://doi.org/10.1097/nen.0000000000000230.
41. Selkoe DJ (2002) Alzheimer's disease is a synaptic failure. *Science* **298**:789–791. https://doi.org/10.1126/science.1074069.
42. Shafiei SS, Guerrero-Muñoz MJ, Castillo-Carranza DL (2017) Tau Oligomers: cytotoxicity, propagation, and mitochondrial damage. *Front Aging Neurosci* **9**:83. https://doi.org/10.3389/fnagi.2017.00083.
43. Smolek T, Madari A, Farbakova J, Kandrac O, Jadhav S, Cente M *et al* (2016) Tau hyperphosphorylation in synaptosomes and neuroinflammation are associated with canine cognitive impairment. *J Comp Neurol* **524**:874–895. https://doi.org/10.1002/cne.23877.
44. Spillantini MG, Goedert M (2013) Tau pathology and neurodegeneration. *Lancet Neurol* **12**:609–622. https://doi.org/10.1016/s1474-4422(13)70090-5.
45. Terry RD (2000) Cell death or synaptic loss in Alzheimer disease. *J Neuropathol Exp Neurol* **59**:1118–1119. https://doi.org/10.1093/jnen/59.12.1118.
46. Terry RD, Masliah E, Salmon DP, Butters N, DeTeresa R, Hill R *et al* (1991) Physical basis of cognitive alterations in Alzheimer's disease: synapse loss is the major correlate of cognitive impairment. *Ann Neurol* **30**:572–580.
47. Usenovic M, Niroomand S, Drolet RE, Yao LH, Gaspar RC, Hatcher NG *et al* (2015) Internalized tau oligomers cause neurodegeneration by inducing accumulation of pathogenic tau in human neurons derived from induced pluripotent stem cells. *J Neurosci* **35**:14234–14250. https://doi.org/10.1523/jneurosci.1523-15.2015.
48. Vyberg M, Nielsen SR (1998) Dextran polymer conjugate two-step visualization system for immunohistochemistry: a comparison of EnVision+ with two three-step avidin-biotin techniques. *Applied Immunohistochemistry* **6**:3–10. https://doi.org/10.1097/00022744-199803000-00002.
49. Wang JZ, Xia YY, Grundke-Iqbal I, Iqbal K (2013) Abnormal hyperphosphorylation of tau: sites, regulation, and molecular mechanism of neurofibrillary degeneration. *J Alzheimers Dis* **33**:S123–S139. https://doi.org/10.3233/jad-2012-129031.

50. Wegiel J, Wisniewski HM, Soltysiak Z (1998) Region- and cell-type-specific pattern of tau phosphorylation in dog brain. *Brain Res* **802**:259–266. https://doi.org/10.1016/s0006-8993(98)00542-3.
51. Weininger J, Roman E, Tierney P, Barry D, Gallagher H, Murphy P *et al* (2019) Papez's forgotten tract: 80 years of unreconciled findings concerning the thalamocingulate tract. *Front Neuroanat* **13**:14. https://doi.org/10.3389/fnana.2019.00014.
52. Woźnicka A, Kosmal A (2003) Cytoarchitecture of the canine perirhinal and postrhinal cortex. *Acta Neurobiol Exp* **63**:197–209.
53. Wu H-Y, Kuo P-C, Wang Y-T, Lin H-T, Roe AD, Wang BY *et al* (2018) β-amyloid induces pathology-related patterns of tau hyperphosphorylation at synaptic terminals. *J Neuropathol Exp Neurol* **77**:814–826. https://doi.org/10.1093/jnen/nly059.
54. Wu XL, Pina-Crespo J, Zhang YW, Chen XC, Xu HX (2017) Tau-mediated neurodegeneration and potential implications in diagnosis and treatment of Alzheimer's disease. *Chin Med J* **130**:2978–2990. https://doi.org/10.4103/0366-6999.220313.
55. Xia D, Li C, Götz J (2015) Pseudophosphorylation of Tau at distinct epitopes or the presence of the P301L mutation targets the microtubule-associated protein Tau to dendritic spines. *Biochim Biophys Acta* **1852**:913–924. https://doi.org/10.1016/j.bbadis.2014.12.017.
56. Youssef SA, Capucchio MT, Rofina JE, Chambers JK, Uchida K, Nakayama H, Head E (2016) Pathology of the aging brain in domestic and laboratory animals, and animal models of human neurodegenerative diseases. *Vet Pathol* **53**:327–348. https://doi.org/10.1177/0300985815623997.
57. Yu CH, Song GS, Yhee JY, Kim JH, Im KS, Nho WG *et al* (2011) Histopathological and immunohistochemical comparison of the brain of human patients with Alzheimer's disease and the brain of aged dogs with cognitive dysfunction. *J Comp Pathol* **145**:45–58. https://doi.org/10.1016/j.jcpa.2010.11.004.
58. Zhu QY, Bi SW, Yao XT, Ni ZY, Li Y, Chen BY *et al* (2015) Disruption of thalamic connectivity in Alzheimer's disease: a diffusion tensor imaging study. *Metab Brain Dis* **30**:1295–1308. https://doi.org/10.1007/s11011-015-9708-7.

SUPPORTING INFORMATION

Additional supporting information may be found in the online version of this article at the publisher's web site:

Table S1. Extended semi-quantitative assessment of S396$^+$ pathology across brain regions in CCD and Non-CCD dogs. S396+ Pathology visualised with EnVision Labelling was semi-quantitatively scored across various substructures in different brain regions. "-" = No Labelling. "+" = Light labelling only in limited areas, some punctate immunoreactivity. "++" = More extensive, stronger labelling, lots of immunoreactive puncta. "+++" = Strong labelling over much of tissue region, strong nuclear associated immunoreactivity, small aggregations present. "++++" Very strong, dense labelling across most of the tissue region, extensive nuclei associated immunoreactivity, lots of aggregations present. Exemplar images of semiquantitative intensity levels are in Figure SX. N/A = Not Available.

Figure S1. Thresholding of S396 EnVision labelling for automated quantitative image analysis exemplar images. (A) RGB image of S396 p-tau labelling in white matter. **(B)** Colour deconvoluted permanent red stain for S396 p-tau image. **(C-E)** Red pixels within a threshold highlighted in red for a range of **(c)** 20-120 "high intensity labelling", **(D)** 20-200 "intermediate intensity labelling", **(E)** 120-220 "lower intensity labelling". **(F)** RGB image of S396 p-tau labelling in white matter. **(g)** Colour deconvoluted permanent red stain for S396 p-tau image. **(H-J)** Red pixels within a threshold highlighted in red for a range of **(H)** 20-120 "high intensity labelling", **(I)** 20-200 "intermediate intensity labelling", **(J)** 120-220 "lower intensity labelling".

Figure S2. Exemplar images for semi-quantitative analysis of S396 pathological severity. "Severity of S396 labelling across regions was assessed semiquantitatively on a five-point scale. Examples of labelling at different levels are illustrated. **0** – no labelling. **1 (+)** sparse punctate labelling in the neuropil, otherwise mostly diffuse or distributed light labelling only (images depict cortical grey matter). **2 (++)** Slightly more intense or more widespread labelling in neuropil, light labelling around some oligodendrocyte nuclei (images depict white matter fascicles travelling transverse to the thalamus, and white matter of the alveus respectively). **3 (+++)** Extensive intense glial aggregations, widespread neuropil labelling and extensive small aggregates and/or punctate labelling (images depict white matter of the temporal lobe and fibre bundles of the mammillothalamic tract respectively). **4 (++++)** same as 3 but with very intense and dense labelling of neuropil (as depicted in images of the stria medullaris and stria terminalis respectively)."

Figure S3. AT8$^-$ no-primary negative control and non-CCD healthy control labelling. Representative images depicting lack of AT8$^+$ immunoreactivity in **(A-B)** Negative no-primary controls of CCD dog canine 3 inferior temporal cortex. **(C-F)** Representative images depicting lack of AT8$^+$ labelling in non-CCD dogs with primary antibodies applied in the **(C)** Inferior temporal cortex, **(D)** Anterior thalamic nucleus, **(E)** Hippocampal formation, **(F)** CA1 stratum pyramidale. Scale bars represent 100 μm unless otherwise marked.

Figure S4. Additional quantitative assessment of ccd and non-ccd dog S396$^+$ p-tau pathology. (A) Densiometric quantification of mean Western blot labelling intensity for different regions in CCD dogs (n=6), with individual data point shown (equivalent of Figure 1A). Statistical results not shown. **(B)** Quantification of tissue area with intermediate level labelling by automated image analysis of EnVision™ labelling. Results of two-way ANOVAs comparing all regions within CCD dogs (n=6) and non-CCD dogs (n=6) as well as comparing between groups for each region are shown. **(C)** Mean area labelled at intermediate intensity threshold across regions of CCD dogs compared to non-CCD dogs. Results of a two-tailed Wilcoxon signed-rank test are shown (P = 0.0078). **(D)** Mean area labelled at low intensity threshold across regions of CCD dogs compared to non-CCD dogs. Results of a two-tailed Wilcoxon signed-rank test are shown (P = 0.0078). All graphs show mean ± SEM, and all statistical analyses were corrected for multiple

comparisons using the FDR method. Full statistical results with corrected and uncorrected p values, t values, degrees of freedom, and Cohen's D are available in Supplementary File 2. ****$P < 0.0001$, ***$P < 0.001$, **$P < 0.01$, *$P < 0.05$ (Int. Caps = Internal Capsule; Hippoc. = Hippocampus; Mam. Bod = Mammillary Body).

Figure S5. Further small-scale micrographs of S396$^+$ p-Tau immunohistochemistry illustrating broader labelling patterns throughout multiple brain regions in CCD dogs. (A) CA3 region from a representative CCD dog, featuring strong labelling in the alveus (Alv), some labelling in the stratum oriens (SO), little to no labelling in the stratum pyramidale (SP), but further immunoreactivity in the stratum radiatum (SR). **(B)** Atypical labelling in the stratum pyramidale of Canine 5, also showing immunoreactivity in the stratum radiatum, and some labelling in the stratum lacunosum-moleculare (SM), but none in the granular cell layer of the dentate gyrus (DG). **(C)** Labelling in the hilus of the dentate gyrus, especially towards the lateral (upper) arm of the granular cell layer. **(D)** Intense labelling observed throughout the fimbria of CCD dogs, especially towards the medial portion (bottom). **(E)** Body of the fornix. **(F)** Anterior thalamic nucleus, including intraneuronal S396+ inclusions in neuronal soma (arrowheads). **(G)** Stria terminalis and dorsal thalamic peduncle. **(H)** Patches of strong punctate immunoreactivity from fascicles of the mammillothalamic tract in cross-section. **(I)** Mediodorsal thalamic nucleus. **(J)** Internal medullary lamina of the thalamus and intraneuronal inclusions in intralaminar nuclei. **(K)** Largely spared ventroanterior nucleus (top left) contrasted with labelling in the external medullary lamina. **(L)** Extensive intra-axonal deposits in the internal capsule. **(M)** Neurons with soma-localised S396 p-tau deposits in Layer II of the temporal cortex of Canine 3, who had AT8$^+$ neurons in the same region. **(N)** Border of the lateral ventricle in the white matter of the temporal cortex including extensive intense perinuclear glial soma deposits. **(O)** Labelling predominantly in the white matter of the occipital cortex, much less intense in more distal parts of the gyri (left) and more intense in deeper white matter (right), a pattern typical of neocortical regions. **(P)** Labelling in cingulate cortex exemplifying more intense immunoreactivity in deeper cortical layers, another pattern typical across neocortical regions. **(Q)** Labelling in frontal cortex including an S396$^+$ immunoreactive apical dendrite approximately 100 μm long. **(R)** Limited immunoreactivity observed in the occipital cortex. **(S)** Strong immunoreactivity in the white matter of the cingulate lobe, including intense perinuclear glial deposits. **(T-U)** Labelling in **(T)** frontal and **(U)** occipital cortical white matter including some small intra-axonal aggregations and lighter perinuclear glial labelling. Scale bar represents 100 μm except where noted.

Figure S6. No-primary and biological negative control immunohistochemical labelling for CCD dogs. (A-L) Representative negative no-primary control labelling from CCD dog brains demonstrating lack of any labelling. All figures chosen to correspond to dogs and regions from main text figures. **(A)** Hippocampal formation. **(B)** CA3 of Canine 5 depicting layers from alveus to granular cell layer of dentate gyrus, equivalent to Figure S5b. **(C)** Fimbria. **(D)** Thalamus. **(e)** Anterior thalamic nucleus. **(F)** Mediodorsal nucleus. **(G)** Internal capsule. **(H-I)** Temporal lobe white matter. **(J)** Cerebellum. **(K)** Deep cerebellar nuclei. **(l)** Cerebellar folia. **(M-O)** Representative negative internal control from CCD dog cerebellum showing lack of positive S396 labelling (with primary antibody against S396 p-tau). Scale bar represents 100 μm except where otherwise specified.

Figure S7. S396$^+$ p-tau immunohistochemistry in healthy control brains. (A) Atypical labelling in the anterior thalamic nuclei of Canine 7 showing low levels of punctate S396$^+$ labelling. **(B)** Labelling typical of non-CCD dogs in the anterior thalamic nuclei of Canine 10, with some weak immunoreactivity in the stria terminalis and lateral ventricle wall, but no positive labelling in the nucleus itself, or the rest of the thalamus. **(C)** Internal capsule of Canine 10. **(A'-C')** Negative no-primary antibody controls of corresponding micrographs. **(D)** Fimbria and CA3 stratum pyramidale of Canine 7, with only weak labelling in the medial portion of the fimbria. **(E)** Fimbria and CA3 stratum pyramidale of Canine 12, showing only immunoreactivity in the medial fimbria. **(F)** CA1 region including alveus, stratum oriens, and stratum pyramidale of Canine 9, the only non-CCD dog to display any immunoreactivity in the hippocampus proper. **(D'-F')** Negative no-primary antibody controls of corresponding micrographs. **(g)** Frontal cortex of Canine 8. **(H)** Cingulum bundle and cingulate cortex of Canine 8. **(I)** Temporal cortical white matter at the border of the lateral ventricle of Canine 8, exhibiting light immunoreactivity seen in some non-CCD dogs. **(G'-I')** Negative no-primary antibody controls of corresponding micrographs. Scale bar represents 100 μm.

Figure S8. Double immunofluorescence with glial markers demonstrates glial nuclei associated S396$^+$ accumulations are not in microglia or astrocytes. (A) Microglial marker Iba-1 (red channel, occipital cortex), **(B)** astrocytic marker GFAP (red channel, occipital cortex). **(A,B)** Show no colocalization between green S396 accumulations and red glial marker, although in **(B)** it appears that two astrocytes may be engulfing a GFAP- S396$^+$ glial soma. Imaged under 60x objective, scale bars represent 20 μm.

Figure S9. S396$^+$ p-tau EnVision™ labelling without hematoxylin counterstain in CCD dog. Micrographs depict a section of hippocampus from CCD Canine 1 with S396$^+$ p-tau labelling with no hematoxylin counterstain, showing accumulations in **(A)** the alveus, and **(B)** the fimbria. Scale bar represents 20 μm.